Some systems require the user to draw bony structures on the source images.(13) While this is an option with our software, it is not required. It is sometimes useful to draw the outline of a bone on both images, and then see how closely they align on the merged image; however, we found that this method significantly increases the burden on the operator. It is generally faster to view the merged portal-DRR image without hand-drawn contours.

Although EPID has become popular, some EPID systems are quite expensive to maintain and have reduced imaging quality. Our software can be used in many situations where good quality EPID is not available.

Because our system uses only three points to calculate the out-of-plane transformation, areas far from the control points (outside the working area) may not align exactly. If the entire image is to be used for alignment, an alternative method would be to use a calibration function such as McalList from the Matrox Imaging Library.(14) With this method, a list of corresponding points on the portal and DRR images is passed to the function and a perspective distortion correction matrix is calculated. The more points that are specified, the more accurate the mapping. However, because only points on the axes can be specified, the corners of the corrected portal image may still be slightly distorted. Specifying many points may also be a burden on the user. An automatic method of detecting all the visible grid tick marks on the portal and DRR images is under investigation.

V. CONCLUSIONS

The ability to estimate offset values improved using our software for the chest phantom that we tested. Setup error estimation was further improved using our automatic error estimation algorithm. Estimations were not statistically different for the pelvis case. Comparing the automatic setup function with a database of clinical cases estimated by human operators revealed that the automatic function works relatively well for head, chest and breast cases, but performs poorly for pelvis and other cases. Automatic registration should improve by increasing the contrast of the portal image. Although setup error can be manually judged accurately and quickly with the software as an aid to doctors and technicians, work remains to make the software more fully automatic.

REFERENCES

1. Hurkmans CW, Remeijer P, Lebesque JV, Mijnheer BJ. Set-up verification using portal imaging: review of current clinical practice. Radiother Oncol. 2001;58(2):105–20.
2. Clippe S, Sarrut D, Malet C, Miquet S, Ginestet C, Carrie C. Patient setup error measurement using 3D intensity-based image registration techniques. Int J Radiat Oncol Biol Phys. 2003;56(1):259–65.
3. Boyer AL. Antonuk L, Fenster A, et al. A review of electronic portal imaging devices (EPIDs). Med Phys. 1992;19(1):1–16.
4. Shirato H, Shimizu S, Kunieda T, et al. Physical aspects of a real-time tumor-tracking system for gated radiotherapy. Int J Radiat Oncol Biol Phys. 2000;48(4):1187–95.
5. Sorcini B and Tilikidis A. Clinical application of image-guided radiotherapy, IGRT (on the Varian OBI platform). Cancer/Radiothér. 2006;10(5):252–57.
6. Pluim J, Maintz J, Viergever M. Mutual-information-based registration of medical images: a survey. IEEE Trans Med Imaging. 2003;22(8):986–1004.
7. Tsao J. Interpolation artifacts in multimodality image registration based on maximization of mutual information. IEEE Trans Med Imaging. 2003;22(7):854–64.
8. Nakashima K, Ashizawa K, Ochi M, et al. Interpretation of normal anatomical structures on chest radiography: comparison of Fuji computed radiography (FCR) 5501D with FCR 5000 and screen-film system. J Appl Clin Med Phys. 2003;4(1):85–90.
9. Yamada S, and Murase K. Effectiveness of flexible noise control image processing for digital portal images using computed radiography. Br J Radiol. 2005;78(930):519–27.
10. Van Sörensen de Koste JR, De Boer HCJ, Schuchhard-Schipper RH, Senan S, Hejimen BJ. Procedures for high precision setup verification and correction of lung cancer patients using CT-simulation and digitally reconstructed radiographs (DRR). Int J Radiat Oncol Biol Phys. 2003;55(3):804–10.

11. Hanley J, Mageras GS, Sun J, Kutcher GJ. The effects of out-of-plane rotations on two dimensional portal image registration in conformal radiotherapy of the prostate. Int J Radiat Oncol Biol Phys. 1995;33(5):1331–43.
12. Dong L, and Boyer A. An image correlation procedure for digitally reconstructed radiographs and electronic portal images. Int J Radiat Oncol Biol Phys. 1995;33(5):1053–60.
13. Lujan AE, Balter JM, Ten Haken RK. Determination of rotations in three dimensions using two-dimensional portal image registration. Med Phys. 1998;25(5):703–08.
14. Matrox Electronic Systems. Matrox imaging library, version 9: user guide. Manual no. Y10513-301-0900. Dorval (HQ), Canada: Matrox Electronic Systems Ltd.; 2008. p. 200–01.

Optimization of fluoroscopy parameters using pattern matching prediction in the real-time tumor-tracking radiotherapy system

2011 Phys. Med. Biol. 56 4803

(http://iopscience.iop.org/0031-9155/56/15/011)

IOP PUBLISHING PHYSICS IN MEDICINE AND BIOLOGY

Phys. Med. Biol. **56** (2011) 4803–4813 doi:10.1088/0031-9155/56/15/011

Optimization of fluoroscopy parameters using pattern matching prediction in the real-time tumor-tracking radiotherapy system

Naoki Miyamoto[1], **Masayori Ishikawa**[1], **Gerard Bengua**[2], **Kenneth Sutherland**[1], **Ryusuke Suzuki**[2], **Suguru Kimura**[3], **Shinichi Shimizu**[3], **Rikiya Onimaru**[3] and **Hiroki Shirato**[3]

[1] Division of Medical Physics and Engineering, Graduate School of Medicine, Hokkaido University, Sapporo, Japan
[2] Department of Medical Physics, Hokkaido University Hospital, Sapporo, Japan
[3] Department of Radiology, Graduate School of Medicine, Hokkaido University, Sapporo, Japan

E-mail: miya-nao@med.hokudai.ac.jp

Received 13 March 2011, in final form 15 June 2011
Published 13 July 2011
Online at stacks.iop.org/PMB/56/4803

Abstract

In the real-time tumor-tracking radiotherapy system, fluoroscopy is used to determine the real-time position of internal fiducial markers. The pattern recognition score (PRS) ranging from 0 to 100 is computed by a template pattern matching technique in order to determine the marker position on the fluoroscopic image. The PRS depends on the quality of the fluoroscopic image. However, the fluoroscopy parameters such as tube voltage, current and exposure duration are selected manually and empirically in the clinical situation. This may result in an unnecessary imaging dose from the fluoroscopy or loss of the marker because of too much or insufficient x-ray exposure. In this study, a novel optimization method is proposed in order to minimize the fluoroscopic dose while keeping the image quality usable for marker tracking. The PRS can be predicted in a region where the marker appears to move in the fluoroscopic image by the proposed method. The predicted PRS can be utilized to judge whether the marker can be tracked with accuracy. In this paper, experiments were performed to show the feasibility of the PRS prediction method under various conditions. The predicted PRS showed good agreement with the measured PRS. The root mean square error between the predicted PRS and the measured PRS was within 1.44. An experiment using a motion controller and an anthropomorphic chest phantom was also performed in order to imitate a clinical fluoroscopy situation. The result shows that the proposed prediction method is expected to be applicable in a real clinical situation.

(Some figures in this article are in colour only in the electronic version)

1. Introduction

The real-time tumor-tracking radiotherapy (RTRT) system was developed (Shirato *et al* 1999) in order to compensate for respiratory-induced motion of tumors. The system consists of a linear accelerator (linac) and two x-ray fluoroscopy systems. In the RTRT system, metal markers are surgically embedded in or near the target tumor. During radiation treatment, the markers are detected by means of continuous fluoroscopy operated at 30 frames s^{-1}. The linac irradiation is only enabled during the period when the detected location of the fiducial marker is within its allowed displacement values with respect to the treatment plan. The location of the inserted fiducial marker is calculated from the projected position in the pair of the fluoroscopic images obtained at two different directions. The marker position on each fluoroscopic image is determined by means of a template pattern matching technique which is based on the normalized cross correlation between the template image and the target image. The pattern recognition score (PRS) is defined by the correlation coefficient. The location that gives the highest PRS is considered to be the marker position in the search area. With high tube voltage, large current and long exposure, the PRS will be higher because a high-signal-to-noise-ratio (SNR) fluoroscopic image can be obtained. In this case, the marker can be tracked accurately and stably; however, the radiation dose due to x-ray fluoroscopy also increases. With many treatment fractions or in long treatment duration of a single fraction, the total imaging dose could be more than what clinically acceptable. On the other hand, by decreasing the fluoroscopy parameter settings, the PRS is decreased and the fiducial marker could be lost. During irradiation, the fluoroscopy parameters such as tube voltage, current and exposure duration are selected manually and empirically. This may result in unnecessary imaging dose from the fluoroscopy or loss of the marker because of too much or insufficient x-ray exposure. Hence, the fluoroscopy parameters have to be adjusted taking into account both the PRS and the fluoroscopic dose.

Optimization of the operating parameters has been investigated and examined in computer tomography (Brisse *et al* 2007, Papadakis *et al* 2008), radiation diagnostic (Doyle *et al* 2005, Ullman *et al* 2006) or mammography (Williams *et al* 2008, Young *et al* 2006). In these radiation diagnostic devices, the optimum tube voltage, current or exposure duration are optimized in consideration of the contrast-to-noise ratio (CNR) or the SNR of the x-ray image. However, the optimization method based on these indices cannot be applied in the RTRT system because the marker moves in various regions of the fluoroscopic image due to respiration. Therefore, it is difficult to determine the relationship between the PRS and the indices of image quality such as CNR or SNR.

In order to minimize the fluoroscopic dose by reducing the pulse rate of the fluoroscopy, various prediction models of tumor movement have been reported (Ruan *et al* 2007, Sharp *et al* 2004). A combination with external signals such as a real-time position management system is also useful for dose reduction (Wu *et al* 2008). Placing an additional filtration material in the fluoroscopic beam (Moore *et al* 2008, Young *et al* 2006) should be useful for the RTRT system. Optimization of the fluoroscopy parameters is one of the best solutions for dose reduction. However, this has not been established yet for the RTRT system.

In the RTRT system, optimization should be focused on reduction of the radiation dose while maintaining the PRS at an acceptable level. For this purpose, we propose a novel optimization method based on prediction of the PRS at an arbitrary position in the fluoroscopic image. In the proposed method, the PRS can be predicted in a region where the marker appears to move in the fluoroscopic image. The predicted PRS can be utilized to judge whether the marker can be tracked with accuracy and stability. Hence, by analyzing the fluoroscopic images obtained in several x-ray tube settings, the best fluoroscopic setting can be derived. This method could be applied not only to the RTRT system but also to other fluoroscopy-based motion tracking systems that use the template pattern matching technique. The purpose of this research is to show the feasibility of the PRS prediction method and to demonstrate the optimization of the fluoroscopy parameters in a phantom study.

2. Materials and methods

2.1. Template pattern matching

In the RTRT system, the fiducial marker is tracked every 0.033 s. On each sequential image, the marker position in the fluoroscopic image is recognized by means of a template pattern matching technique. The template image of the fiducial marker has to be registered in advance. In the RTRT system, the fluoroscopic image of the fiducial marker which is captured before insertion into the patients is used as the template image. In general, the same template image is applied to all treatments because the markers are manufactured with same specification. Template pattern matching is based on normalized cross correlation. The correlation coefficient is given by

$$r = \frac{N\sum_{i=1}^{N} I_i M_i - \left(\sum_{i=1}^{N} I_i\right)\sum_{i=1}^{N} M_i}{\sqrt{\left|N\sum_{i=1}^{N} I_i^2 - \left(\sum_{i=1}^{N} I_i\right)^2\right|\left|N\sum_{i=1}^{N} M_i^2 - \left(\sum_{i=1}^{N} M_i\right)^2\right|}}, \tag{1}$$

where N is the pixel number, and I_i and M_i are the pixel values of the target image and the template image, respectively. The target image has to be cropped from the fluoroscopic image with the same size of the template image. The PRS is defined as

$$\mathrm{PRS} = \begin{cases} 0 & (r < 0), \\ 100 \times r^2 & (r \geqslant 0). \end{cases} \tag{2}$$

In our case, we are not interested in the negative value, so results are clipped to 0. The location that gives the highest PRS is considered to be the marker position in the search area. Other algorithms for determining the marker position have also been considered; however, they are not discussed in this paper.

In order to avoid the misidentification of the marker and to track only the marker, the threshold value of the PRS should be determined beforehand. If the maximum PRS in the search area is greater than the threshold value, the location that gives the highest PRS is considered to be the marker position. On the other hand, in case the maximum PRS is lower than the threshold value, the system decides that no markers are within the search area. If a high threshold value is applied, tracking accuracy is improved; however, the probability of losing the track of the marker is also increased. If a low threshold is used, the probability of the marker misidentification is increased. Hence, we must adjust the threshold value taking into account both tracking accuracy and stability.

The PRS depends on the quality of the fluoroscopic images. Assuming that a stable marker is tracked with the same exposure condition, the PRS fluctuates on each sequential image in fluoroscopy. This is mainly caused by the statistical noise of a digital x-ray image

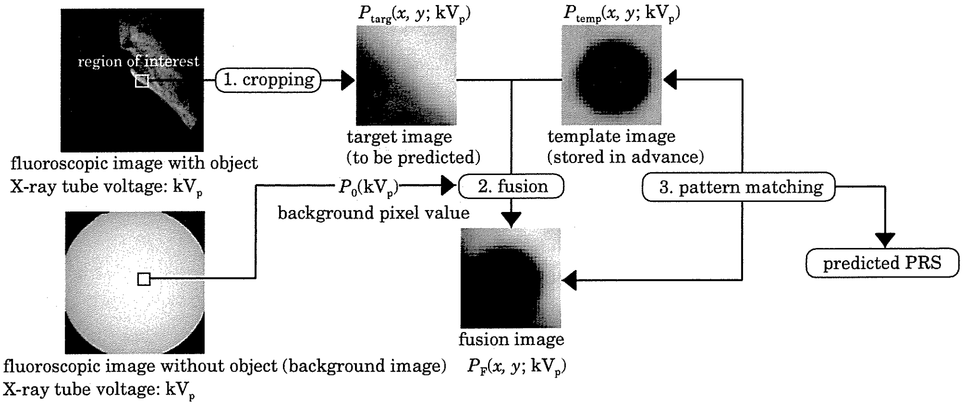

Figure 1. Outline of the pattern recognition score (PRS) prediction method.

(e.g. quantum noise, electronic noise). In a higher SNR image, the fluctuation of the PRS is smaller. Fluctuation of the PRS is correlated with that of the projected marker position in the fluoroscopic images. The 3D marker coordinates calculated by the RTRT system are also altered according to these fluctuations. The fluctuation of the 3D coordinates can be regarded as the tracking accuracy. As a result, the PRS can be one of the indicators of tracking accuracy. The relationship between the PRS and the tracking accuracy will depend on the characteristics of the imaging devices of the fluoroscopy system. Therefore, the relationship should be investigated in order to assure tracking accuracy for each system.

2.2. *PRS prediction algorithm*

The outline of the PRS prediction method is shown in figure 1. For simplicity, the parameter for optimization is assumed to be the x-ray tube voltage, kV_p. Other parameters, tube current and exposure duration, can be optimized in the same manner. The proposed prediction algorithm is a three-step procedure. First, the target area for PRS prediction is cropped from the fluoroscopic image with the same size as that of the template image. The pixel value distribution of the template image and the cropped target area obtained in a specific x-ray tube voltage kV_p are defined as $P_{temp}(x, y; kV_p)$ and $P_{targ}(x, y; kV_p)$, respectively. An x-ray attenuation factor for each pixel position is calculated by taking into account the pixel value of the background image which is obtained without the objects. The background images should be obtained for each exposure setting in advance. The attenuation factor distributions of the template image and the target image are defined as

$$A_{temp}(x, y; kV_p) = -\ln\frac{P_{temp}(x, y; kV_p)}{P_0(kV_p)}, \tag{3}$$

$$A_{targ}(x, y; kV_p) = -\ln\frac{P_{targ}(x, y; kV_p)}{P_0(kV_p)}, \tag{4}$$

where $P_0(kV_p)$ is defined as the average pixel value of the background image. In order to consider the ununiformity of the background image, the location of the background image is selected according to the position where the template image is placed. Second, a fused image

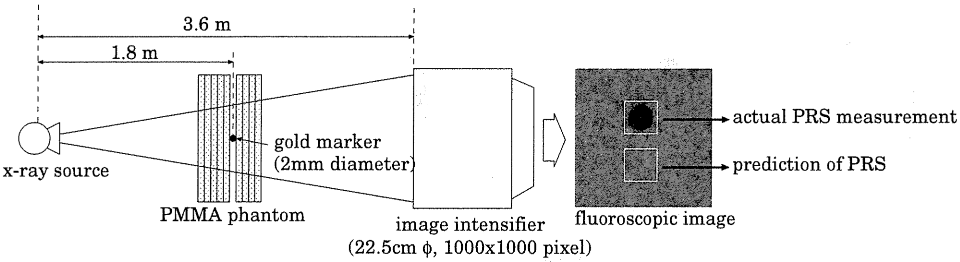

Figure 2. Experimental setup for examination of the relationship between the PRS and the tracking accuracy. This same setup was used for verification of the PRS prediction algorithm.

is constructed by assuming that the marker is within the cropped area. By considering the x-ray attenuation factor, the predicted pixel value distribution can be expressed as

$$P_F(x, y; \mathrm{kV_p}) = P_0(\mathrm{kV_p}) \exp\{-A_{\mathrm{temp}}(x, y; \mathrm{kV_p}) - A_{\mathrm{targ}}(x, y; \mathrm{kV_p})\}, \qquad (5)$$

where the $P_F(x, y; \mathrm{kV_p})$ is the pixel value distribution of the predicted fusion image. Finally, the predicted PRS value is calculated by performing template pattern matching between the fused image $P_F(x, y; \mathrm{kV_p})$ and the template image $P_{\mathrm{temp}}(x, y; \mathrm{kV_p})$. In principle, the beam-hardening effect should be considered in order to construct the actual fusion image. The x-ray units used in this study have a filtration material which can remove the low-energy x-ray. Hence, the beam-hardening effect is no longer considered in this study. The effect of beam-hardening is to be addressed in future work.

The PRS at an arbitrary position in the fluoroscopic image can be predicted by the above procedures. By predicting the PRS in a region where the fiducial marker is expected to move in the fluoroscopic image, the tracking accuracy and stability can be evaluated without additional fluoroscopic dose. By processing the images obtained in different fluoroscopy settings, the optimum condition that gives the minimum fluoroscopic dose while maintaining the tracking accuracy at an acceptable level can be determined.

2.3. Experiments

2.3.1. Relationship between the tracking accuracy and the PRS. First, the relationship between the PRS and the fluctuation of the measured 3D coordinates of the fiducial marker was investigated. The experimental setup is illustrated in figure 2. The distance between the x-ray source and the x-ray image intensifier (I.I.) was fixed at 3.6 m. The I.I. had an input of 22.5 cm diameter and was coupled to a 1000 × 1000 pixel resolution CCD camera. A 2.0 mm ∅ gold fiducial marker was placed at the isocenter and was sandwiched by polymethylmethacrylate (PMMA) slabs which have an area of 300 mm × 400 mm. In order to vary the PRS, the total thickness of the PMMA phantom was varied between 40 and 200 mm. Under each exposure condition, both the PRS and the recognition position on the fluoroscopic image were recorded 100 times every 0.033 s. The standard deviation (SD) of the recorded 100 recognition positions was converted to the SD of the 3D marker coordinates. The SD of the 3D marker coordinates should correspond to the tracking accuracy. Hence, the relationship between the PRS and the tracking accuracy was derived from this experiment.

2.3.2. Verification of the PRS prediction. Verification of the PRS prediction was performed with the same geometry as shown in figure 2. The tube current and tube exposure time were

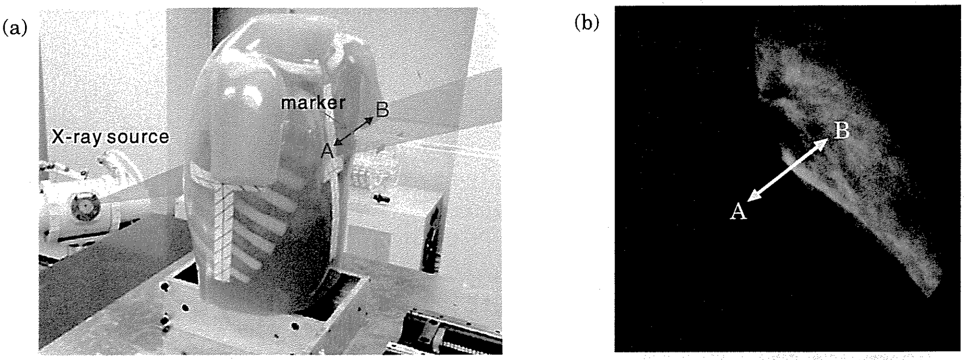

Figure 3. (a) Experimental setup for the phantom study. (b) An example of the x-ray fluoroscopic image. The marker was moved linearly between A and B.

fixed to 80 mA and 3 ms, respectively. By assuming that the image quality around the marker should be the same, the PRS was predicted from the area near the actual marker position as shown in figure 2. The template images and the background images, which corresponded to $P_{\mathrm{temp}}(x, y; \mathrm{kV_p})$ and $P_0(\mathrm{kV_p})$, respectively, were recorded in each experimental x-ray tube voltage in advance. The experiment involved two scenarios. The first case was a variable x-ray tube voltage ranging from 40 to 90 $\mathrm{kV_p}$ with 2 $\mathrm{kV_p}$ increment, and fixed PMMA thickness of 80 mm. The PMMA thickness of 80 mm was assumed to be equal to an imaging condition of lung fluoroscopy. The second case was a fixed tube voltage of 50 $\mathrm{kV_p}$ and the variable PMMA thickness ranging from 0 to 180 mm. The increment of the thickness was 20 mm. The PMMA thickness of 180 mm was assumed to be equal to a typical patient thickness (Vano *et al* 2006). The PMMA thickness was varied in order to imitate the marker overlapped in the variable density including the lung, bone and so on. It was confirmed in advance that the minimum tube voltage to recognize the marker was around 50 $\mathrm{kV_p}$ in this PMMA thickness range. In order to consider the fluctuation of the measured PRS and the predicted PRS, the fluoroscopic image was acquired ten times on each exposure setup. The measured and the predicted PRS were compared to assess the prediction accuracy.

2.3.3. Phantom study. In order to confirm the accuracy of the PRS prediction in a clinical fluoroscopy situation, an experiment using a motion controller and an anthropomorphic chest phantom was performed. The experimental setup is shown in figure 3(a). Alignment of the x-ray tube and the I.I. was the same as in the previous experiments. The marker was placed in front of the phantom and was moved using the motion controller to mimic respiratory marker motion. The marker was moved linearly in the left–right direction of the phantom with a speed of 10 $\mathrm{mm\,sec^{-1}}$. In the obtained fluoroscopic images, the marker moved within a region of varying media which included the lung, bone and heart. An example of the fluoroscopic image is shown in figure 3(b). The white arrow indicates the marker trajectory in the fluoroscopic image. The motion of the marker was tracked using the RTRT system, and both the PRS and the recognized position were recorded every 0.033 s. The x-ray tube voltage was varied from 46 to 54 $\mathrm{kV_p}$ with 2 $\mathrm{kV_p}$ increments. The tube current and exposure time were fixed to 80 mA and 3 ms, respectively. After gathering the sets of PRS and recognized positions along the marker trajectory, an image was captured without the marker. The fluoroscopic image

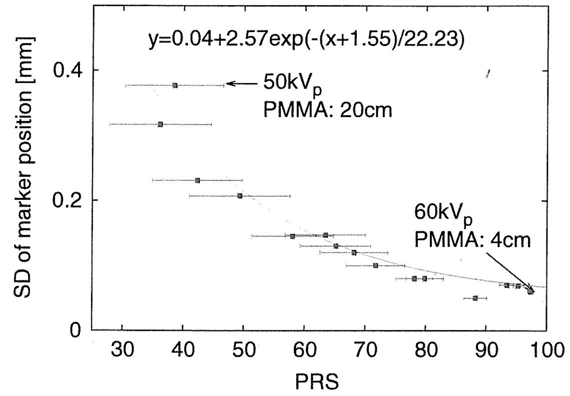

Figure 4. Relationship between the PRS and the SD of the 3D marker location. The solid line is a fitting curve.

without the marker was used for PRS prediction. The measured PRS and the predicted PRS were compared for each tube voltage.

3. Results

3.1. Relationship between the tracking accuracy and the PRS

The relationship between the PRS and the SD of the 3D marker coordinates is shown in figure 4. The horizontal error bars represent the SD of the PRS in 100 times measurements under the same exposure condition. That was mainly caused by the statistical noise of the fluoroscopic image. In the case of large thickness of PMMA or low tube voltage, the PRS was decreased because of the low SNR of the image. In addition, the SD of the PRS was increased for the same reason. The marker was not able to be recognized correctly in the PRS region below 30. In contrast, the PRS was increased with thinner PMMA or high tube voltage. The PRS never reached 100 because an image that is exactly same as the template image is not able to be observed in the fluoroscopic image due to statistical noise of the image.

Curve fitting was applied in order to define the relationship between the PRS and the SD of the 3D coordinates. The SD is regarded as the tracking accuracy. In our experiment, it was found that the tracking accuracy could be kept within about 0.1 mm when the PRS exceeds about 75 during the marker tracking. It was almost equal to imaging resolution. Hence, the threshold PRS of 75 was considered to be suitable for accurate marker tracking in our experimental setup.

3.2. Verification of the prediction method

The result of variable x-ray tube voltage with fixed PMMA thickness of 80 mm is shown in figure 5(a). Each point represents 2 kV$_p$ increments. The predicted PRS showed good agreement with the measured PRS. The SD of both the prediction and the measurement in the high PRS region was found to be smaller than that of the low-PRS region. The SD depended on the image quality as mentioned above. By taking account of the 2kV increment, it was found that the PRS decreased drastically at a typical x-ray tube voltage. Hence, it would be difficult to determine the optimum tube voltage by manual operation. In order to evaluate the

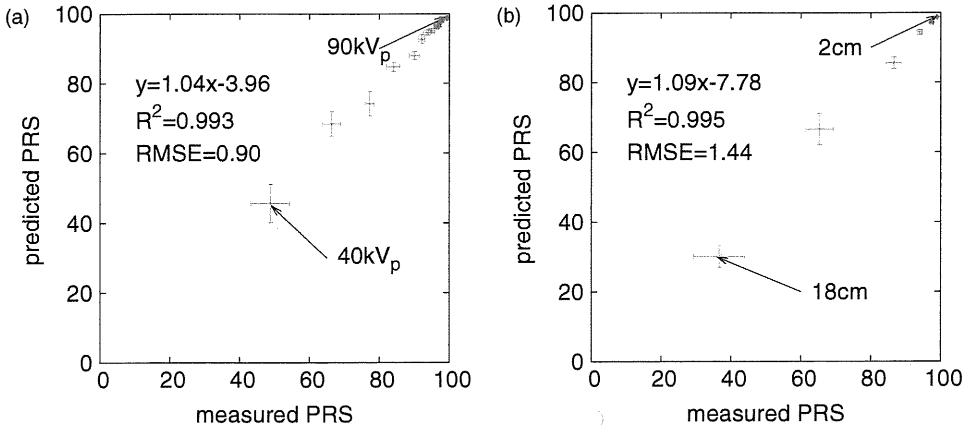

Figure 5. Measured and predicted PRS: (a) constant thickness and variable tube voltage and (b) constant tube voltage and variable thickness.

prediction accuracy, the coefficient of determination R^2 was derived from linear regression between the predicted PRS and the measured PRS. The root mean square error (RMSE) was also calculated as a prediction error. In the case of variable x-ray tube voltage and fixed PMMA thickness, $R^2 = 0.993$ and RMSE $= 0.90$ were obtained. The relationship between the predicted PRS and the measured PRS showed good linearity. In addition, the RMSE was within the statistical error. Hence, the PRS could be predicted within acceptable discrepancy in the case of variable x-ray tube voltage.

The result of variable PMMA thickness with fixed tube voltage of 50 $\mathrm{kv_p}$ is shown in figure 5(b). The SD of both the measured PRS and the prediced PRS was increased as PMMA thickness was increased. In this case, $R^2 = 0.995$ and RMSE $= 1.44$ were obtained. The RMSE was larger compared with the result of fixed PMMA thickness. One of the reasons was assumed to be the beam-hardening effect. However, the prediction error could be mainly caused by the statistical noise as mentioned above. Hence, the discrepancy between the measured PRS and the predicted PRS could be permissible. It was confirmed that the proposed method can predict the PRS in both cases of varying tube voltage and varying object thickness. The patient's couch will be overlapped in the fluoroscopic images in the actual clinical case. The effect of the x-ray absorbance by the couch is to be addressed in future work.

3.3. Phantom study

The results of the measured PRS and the predicted PRS along the marker trajectory for each x-ray tube voltage are shown in figure 6. The measured PRS and the predicted PRS showed the same trend for each tube voltage. The RMSE was decreased as the tube voltage was increased. This was mainly caused by the improvement of the SNR. As shown in figure 3(b), region A was a thick region which included the heart and bone. Region B was less dense compared to region A, including only the lung region. The SNR of the fluoroscopic image captured in region A should be lower than that of region B. Hence, the PRS of region A was relatively low compared to that of region B.

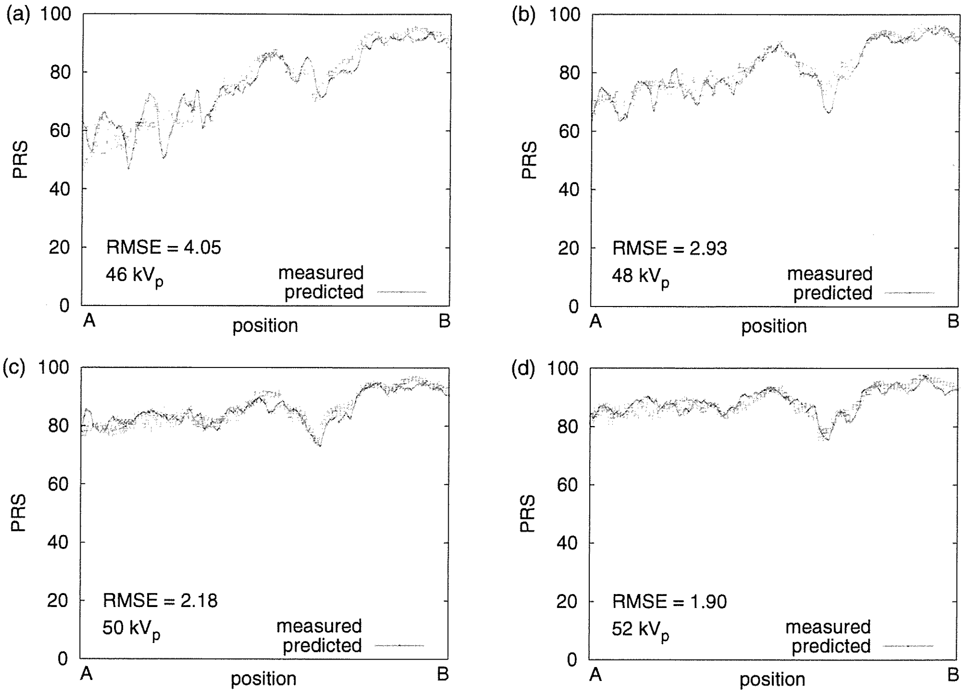

Figure 6. Measured and predicted PRS for each x-ray tube voltage: (a) 46 kV$_p$, (b) 48 kV$_p$, (c) 50 kV$_p$ and (d) 52 kV$_p$.

The PRS at the boundary between region A and region B could not be improved even if the tube voltage was increased. One reason was that the brightness of the target image in the border area was clearly separated. In our experiments, the predicted PRS showed the same trend as the measured PRS along the marker trajectory including the border region. In the clinical situation, the fluoroscopic images contain a large variation of the pixel value distribution. Hence, the proposed prediction method is expected to be applicable in a real clinical situation.

4. Discussion

The optimization procedure based on PRS prediction is discussed by taking an example from the results of the phantom study. For the purpose of optimization, the pass-rate is defined as a ratio of the number of the points that exceed the threshold PRS and the number of all points. The threshold PRS of 75, which corresponds to about 0.1 mm tracking accuracy, was applied in the analysis. The RMSE and pass-rate are summarized in table 1. The predicted pass-rate showed good agreement with the measured pass-rate. The difference between the measured and the predicted pass-rate was within 2.3% in our experiments. The tube parameters are optimized when the pass-rate is almost 100%. The optimum tube voltage was estimated to be either 50 kV$_p$ or 52 kV$_p$ in our fluoroscopic setup. Tube parameters, such as current and exposure time, can also be optimized in the same manner. Thus, the best fluoroscopic condition can be derived by analyzing the images captured in different tube settings.

Table 1. RMSE and the pass-rate for each tube voltage.

Tube voltage (kV_p)	RMSE of PRS	Pass-rate (%)	
		Measured	Predicted
46	4.05	50.7	48.4
48	2.93	71.6	73.1
50	2.18	98.4	97.1
52	1.90	100.0	99.7
54	1.83	100.0	100.0

It has been reported that the skin surface dose rate from RTRT could be as high as 1 $Gy\,h^{-1}$ (Shirato *et al* 2000b). The exposure time of the fluoroscopy could extend for more than 30 min in a specific case such as irregular motion of the tumor. Assuming the worst case, the cumulative dose due to the fluoroscopy could reach an unacceptable value of 1Gy, which is referenced as a limit level in interventional radiology (Vano *et al* 2009). Hence, the optimization of the fluoroscopic parameters is strongly required for dose reduction. For example, a nominal x-ray tube voltage from 90 kV_p to 110 kV_p, tube current of 100 mA and pulse width of 4 ms are used in the actual RTRT irradiation of the lung region. The experimental setup for this study was based on actual lung treatments. It was shown that the tube voltage can be reduced to the minimum value while maintaining the PRS at an acceptance level. For example, if the tube voltage can be reduced from 90 kV_p to 50 kV_p, the fluoroscopic dose can be reduced by about 80%. Hence, the imaging dose could be reduced significantly by the proposed method.

By reducing the tube voltage manually at small increments while tracking the marker, the optimum tube voltage may be defined. In manual operation, however, the marker should be tracked for a long time, which includes many respiratory cycles, in order to confirm the tracking stability. This is because the marker does not always move on the same trajectory. Hence, more time and additional dose are needed for manual optimization. In contrast, our proposed method can predict the PRS at an arbitrary position where the marker is expected to move. The optimized fluoroscopy condition can be determined quickly by considering whether or not the predicted pass-rate is acceptable. In actual treatment, respiration affects both the motion of the marker and the adjacent organs. Hence, the PRS should be predicted in the region of the marker trajectory including an additional margin.

If the digitally reconstructed radiographs (DRRs), which are reconstructed by a planning computer tomography (CT), can be used as the fluoroscopic images, the pseudo-target could be created by adding the template images and the background images to the DRRs without the actual fluoroscopic images. However, problems such as the resolution of the CT images, the inconsistency of the imaging condition between the CT and the fluoroscopy and so on should be solved.

5. Conclusion

A technique for the optimization of x-ray fluoroscopy in the RTRT system was investigated. It was confirmed that the proposed method can predict the PRS in both cases of varying tube voltage and varying object thickness. In addition, the optimum fluoroscopy parameter was derived while keeping the PRS high enough to track the marker accurately. As a result, the proposed optimization method based on PRS prediction can be applicable in the RTRT system.

This method could also be used for other systems that use the motion tracking technique based on template pattern matching.

Acknowledgments

A part of this research is granted by the Japan Society for the Promotion of Science (JSPS) through the 'Funding Program for World-Leading Innovative R&D on Science and Technology (FIRST Program)' initiated by the Council for Science and Technology Policy (CSTP). A part of this work belongs to 'Research and Development Project on Treatment Equipment Using High Accurate X-Ray Radiation' which Hokkaido University contracted with New Energy and Industrial Technology Development Organization (NEDO).

References

Brisse H J, Madec L, Gaboriaud G, Lemoine T, Savignoni A, Neuenschwander S, Aubert B and Rosenwald J C 2007 Automatic exposure control in multichannel CT with tube current modulation to achieve a constant level of image noise: experimental assessment on pediatric phantoms *Med. Phys.* 34 3018–33

Doyle P, Martin C J and Gentle D 2005 Dose-image quality optimisation in digital chest radiography *Radiat. Prot. Dosim.* 114 269–72

Moore C S, Beavis A W and Saunderson J R 2008 Investigation of optimum x-ray beam tube voltage and filtration for chest radiography with a computed radiography system *Br. J. Radiol.* 81 771–7

Papadakis A E, Perisinakis K and Damilakis J 2008 Automatic exposure control in pediatric and adult multidetector CT examinations: a phantom study on dose reduction and image quality *Med. Phys.* 35 4567–76

Ruan D, Fessler J A and Balter J M 2007 Real-time prediction of respiratory motion based on local regression methods *Phys. Med. Biol.* 52 7137–52

Sharp G C, Jiang S B, Shimizu S and Shirato H 2004 Prediction of respiratory tumour motion for real-time image-guided radiotherapy *Phys. Med. Biol.* 49 425–40

Shirato H *et al* 2000b Physical aspects of a real-time tumor-tracking system for gated radiotherapy *Int. J. Radiat. Oncol. Biol. Phys.* 48 1187–95

Shirato H, Shimizu S, Shimizu T, Nishioka T and Miyasaka K 1999 Real-time tumor-tracking radiotherapy *Lancet* 353 1331–2

Ullman G, Sandborg M, Dance D R, Hunt R A and Alm Carlsson G 2006 Towards optimization in digital chest radiography using Monte Carlo modelling *Phys. Med. Biol.* 51 2729–43

Vano E *et al* 2009 Patient dose reference levels for interventional radiology: a national approach *Cardiovasc. Intervent. Radiol.* 32 19–24

Vano E, Gonzalez L, Fernandez J M, Prieto C and Guibelalde E 2006 Influence of patient thickness and operation modes on occupational and patient radiation doses in interventional radiology *Radiat. Prot. Dosim.* 118 325–30

Williams M B *et al* 2008 Optimization of exposure parameters in full field digital mammography *Med. Phys.* 35 2414–23

Wu H, Zhao Q, Berbeco R I, Nishioka S, Shirato H and Jiang S B 2008 Gating based on internal/external signals with dynamic correlation updates *Phys. Med. Biol.* 53 7137–50

Young K C, Oduko J M, Bosmans H, Nijs K and Martinez L 2006 Optimal beam quality selection in digital mammography *Br. J. Radiol.* 79 981–90

Int. J. Radiation Oncology Biol. Phys., Vol. 81, No. 3, pp. 871–879, 2011

0360-3016/$ - see front matter

ELSEVIER

doi:10.1016/j.ijrobp.2010.11.078

PHYSICS CONTRIBUTION

ACCURATE ANALYSIS OF THE CHANGE IN VOLUME, LOCATION, AND SHAPE OF METASTATIC CERVICAL LYMPH NODES DURING RADIOTHERAPY

SEISHIN TAKAO, PH.D.,* SHIGERU TADANO, PH.D.,* HIROSHI TAGUCHI, M.D., PH.D.,† KOICHI YASUDA, M.D.,† RIKIYA ONIMARU, M.D., PH.D.,† MASAYORI ISHIKAWA, PH.D.,‡ GERARD BENGUA, PH.D.,‡ RYUSUKE SUZUKI, PH.D.,‡ AND HIROKI SHIRATO, M.D., PH.D.†

*Graduate School of Engineering, †Graduate School of Medicine, and ‡Department of Medical Physics, Hokkaido University, Sapporo, Japan

Purpose: To establish a method for the accurate acquisition and analysis of the variations in tumor volume, location, and three-dimensional (3D) shape of tumors during radiotherapy in the era of image-guided radiotherapy.
Methods and Materials: Finite element models of lymph nodes were developed based on computed tomography (CT) images taken before the start of treatment and every week during the treatment period. A surface geometry map with a volumetric scale was adopted and used for the analysis. Six metastatic cervical lymph nodes, 3.5 to 55.1 cm^3 before treatment, in 6 patients with head and neck carcinomas were analyzed in this study. Three fiducial markers implanted in mouthpieces were used for the fusion of CT images. Changes in the location of the lymph nodes were measured on the basis of these fiducial markers.
Results: The surface geometry maps showed convex regions in red and concave regions in blue to ensure that the characteristics of the 3D tumor geometries are simply understood visually. After the irradiation of 66 to 70 Gy in 2 Gy daily doses, the patterns of the colors had not changed significantly, and the maps before and during treatment were strongly correlated (average correlation coefficient was 0.808), suggesting that the tumors shrank uniformly, maintaining the original characteristics of the shapes in all 6 patients. The movement of the gravitational center of the lymph nodes during the treatment period was everywhere less than ±5 mm except in 1 patient, in whom the change reached nearly 10 mm.
Conclusions: The surface geometry map was useful for an accurate evaluation of the changes in volume and 3D shapes of metastatic lymph nodes. The fusion of the initial and follow-up CT images based on fiducial markers enabled an analysis of changes in the location of the targets. Metastatic cervical lymph nodes in patients were suggested to decrease in size without significant changes in the 3D shape during radiotherapy. The movements of the gravitational center of the lymph nodes were almost all less than ±5 mm. © 2011 Elsevier Inc.

Adaptive radiotherapy, Tumor deformation, Tumor geometry, Image-guided radiotherapy, Intensity-modulated radiation therapy.

INTRODUCTION

The latest advances in high-precision radiotherapy enable focusing of higher radiation doses to the tumor region while minimizing unwanted radiation exposure to surrounding tissue. Intensity-modulated radiation therapy (IMRT) varies the intensities and profiles of beams from various directions to fit the tumor size and shape. An initial treatment plan prescribing the radiation field and dose in IMRT is made based on information about the tumor location and geometry before treatment starts. If the tumor moves or shrinks during treatment, the surrounding normal tissue may become included in the region exposed to high radiation doses (1). Such potential anatomic changes can be measured and corrected during fractionated radiotherapy by any of several imaging techniques. Image-guided radiotherapy (IGRT) is one such technique for margin reduction caused by setup uncertainties or anatomic movement used to improve the accuracy of dose delivery. Many studies have reported interfractional organ motions and targeting errors in IGRT using daily computed tomography (CT) images (2–4). The clinical efficacy of IGRT techniques in reducing the treatment margins have been confirmed in head-and-neck cancer (5–7) and prostate cancer (8–10).

However, it is still not practical to perform daily modifications to treatment plans to adapt to observed changes in

---

Reprint requests to: Seishin Takao, Ph.D., Division of Human Mechanical Systems and Design, Graduate School of Engineering, Hokkaido University, N13 W8, Kita-ku, Sapporo, 060-8628, Japan. Tel: (+81) 11-706-6406; Fax: (+81) 11-706-6406; E-mail: takao@mech-me.eng.hokudai.ac.jp

Supported in part by a Grant-in-Aid for Scientific Research (A), MEXT (NO. 18209039) and Grant-in-Aid for JSPS Fellows (NO. 09J02587).

Conflict of interest: none.

Received March 25, 2010, and in revised form Oct 21, 2010. Accepted for publication Nov 29, 2010.

Table 1. Characteristics of the patients

Characteristic	Patient 1	2	3	4	5	6
Sex	F	M	F	M	M	M
TMN classification	T2bN2M0	T3N2M0	T3N2M0	T2bN1M0	T3N2M0	T1N1M0
Pathologic type						
Undifferentiated carcinoma /Squamous cell carcinoma	Undiff	Undiff	SqCC	Undiff	SqCC	Undiff
Treatment						
IMRT/Conventional RT (Conv)	IMRT	Conv	IMRT	IMRT	IMRT	IMRT
Dose (Gy)						
Total dose and number of fractions (fr)	66 (33 fr)	70 (35 fr)	70 (35 fr)	70 (35 fr)	70 (35 fr)	66 (33 fr)
Initial tumor volume (cm^3)	3.5	55.1	10.4	7.6	7.2	12.7

Abbreviations: Undiff = undifferentiated carcinoma; SqCC = squamous cell carcinoma; IMRT = intensity-modulated radiation therapy; RT = radiation therapy; Conv = conventional; fr = fractions.

the tumor dimensions. Several practical ways to minimize anatomic uncertainties have been reported. Hansen *et al.* proposed a strategy of repeated CT imaging and replanning to ensure adequate doses to the target volumes and safe doses to normal tissue during the course of IMRT (11). Smyth *et al.* verified the dose coverage in clinical target volumes at the time of treatment delivery using a dose distribution overlay technique (12). Several image registration methods have also been proposed for online replanning in IGRT (13–16). To improve the efficacy of practical solutions, accumulation of precise knowledge about the changes in tumor volumes, locations, and especially the three-dimensional (3D) shape during radiotherapy is critically important. The authors have proposed a method to

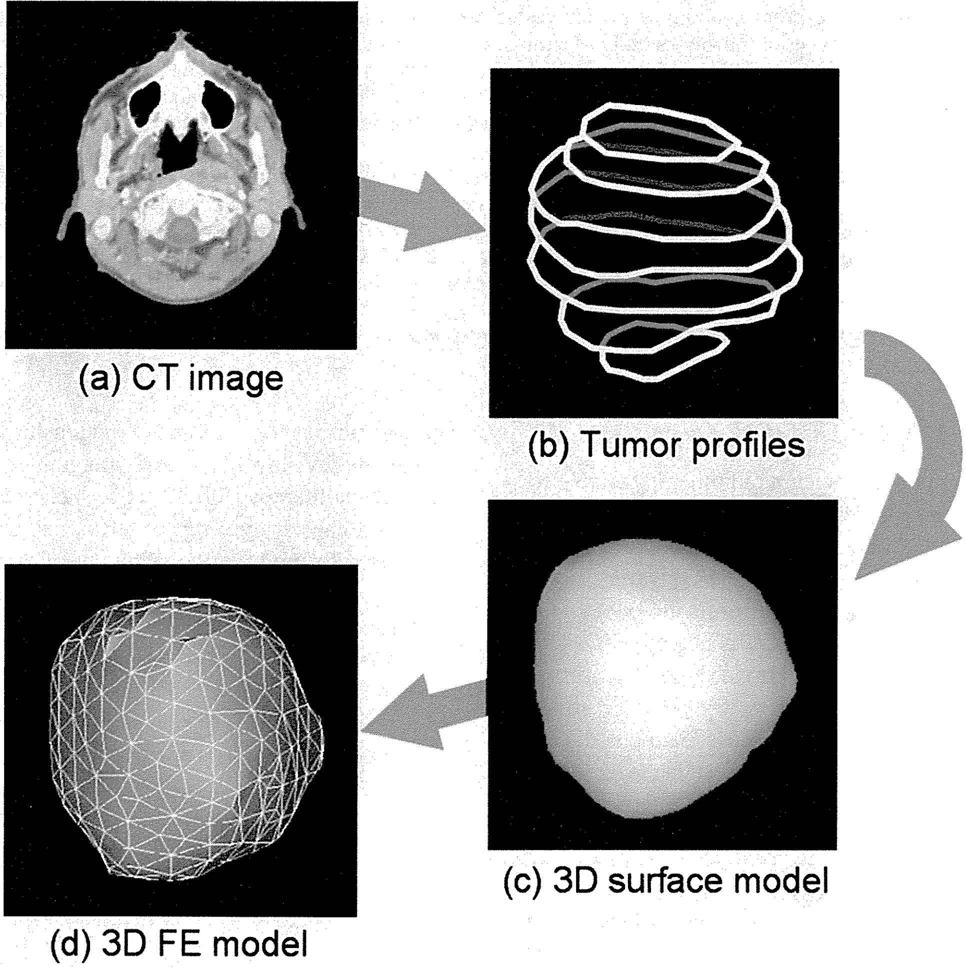
(a) CT image

(b) Tumor profiles

(c) 3D surface model

(d) 3D FE model

Fig. 1. Finite element modeling process for the tumors. (a) CT image for treatment planning. (b) Tumor contours on each slice. (c) 3D surface model of the tumor. (d) Finite element (FE) model of the tumor.

represent 3D tumor shapes in a two-dimensional (2D) map and evaluate the therapeutic response to radiotherapy (17).

The purpose of this study was to establish an accurate method for the acquisition and analysis of variations in tumor volumes, locations, and 3D shapes during radiotherapy. The 3D tumor geometry was expressed in terms of distances from the tumor center to the tumor boundary. This information is represented in 2D color-scaled maps of the distances from the center, from which the 3D tumor shapes can be visually and quantitatively assessed. Further, by comparison of maps before and after treatment, the therapeutic response can be evaluated quantitatively based on the changes in tumor shape during the course of treatments.

METHODS AND MATERIALS

Clinical cases

The study participants were 6 patients with nasopharyngeal cancer and metastatic cervical lymph nodes who were treated at the Hokkaido University Hospital, Sapporo, Japan, between February 2007 and November 2008. The patient characteristics are given in Table 1. Of the 6 patients, 3 had Stage T3N2M0 disease, and 3 patients were diagnosed with Stages T2bN2M0, T2bN1M0, and T1N1M0 disease, respectively. Four tumors were undifferentiated carcinomas and two were squamous cell carcinomas. The average target volume was 16.1 cm^3 (range, 3.5–55.2 cm^3). All the patients except the patient with the largest lymph node (Patient 2) were treated with IMRT; Patient 2 received conventional radiotherapy. The dose distribution before radiotherapy intended each node in this study to be homogeneously irradiated with a dose of 66 to 70 Gy in 2 Gy fractions delivered five times a week.

Pretreatment CT images (CT0) were taken for the treatment planning. The slice thickness of the pretreatment CT images was 2 mm. After the start of treatment, follow-up CT images were taken at weekly intervals (CT1, CT2, CT3, etc). The slice thickness of the follow-up CT images was 5 mm. All patients were immobilized by thermoplastic masks during the CT scanning and treatment. Additionally, in the head-and-neck IMRT treatments in our hospital, a mouthpiece with three fiducial markers (2-mm diameter gold pellets) was used in the fluoroscopic verification of the patient setup (18). This study was conducted with written informed consent

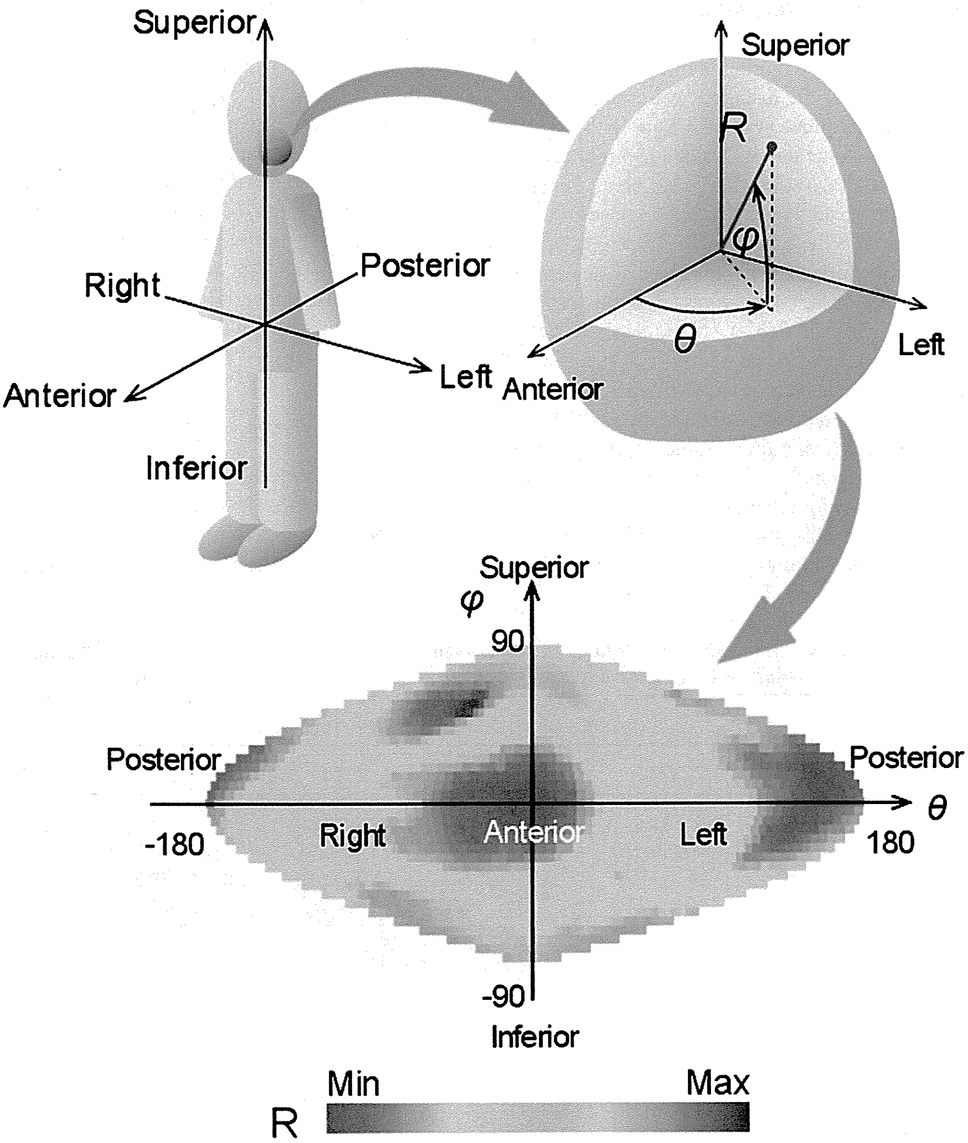

Fig. 2. Representation of the three-dimensional tumor geometry in a two-dimensional color map (surface geometry map).

obtained from all patients and was approved by the institutional ethical committee at Hokkaido University Hospital.

Finite element models of metastatic lymph nodes

Finite element (FE) models of the targets were constructed based on the tumor images. The procedure is shown in Fig. 1. One radiation oncologist (H. T.) determined and contoured metastatic cervical lymph nodes on the CT images with appropriate window settings by means of a radiotherapy planning system (Xio, Computerized Medical Systems, St. Louis, MO) (Fig. 1a). A group of sequential cross-sectional profiles of the tumor were then loaded into biomedical imaging software (Analyze PC 7.0, Mayo Foundation, Rochester, MN) and interpolated to 1-mm intervals (Fig. 1b). From these images, 3D surface models of the tumors were constructed and saved in DXF (Drawing Exchange Format) (Fig. 1c), and the DXF files were converted to IGES (Initial Graphics Exchange Specification) files. Finally, the IGES files were imported into the finite element analysis software package (ANSYS 11.0, ANSYS, Canonsburg, PA), and then the 3D FE models of the tumors were constructed (Fig. 1d).

Evaluation of tumor geometry and location

The quantitative evaluation of the 3D tumor geometry was performed using the distances from the tumor center to its surface at every angle (17). The values of the distances were represented by the radius R in a spherical coordinate system $O\text{-}R\theta\varphi$, with the origin set at the center of gravity of the tumor. The angle θ represents the azimuthal angle ($-180° \leq \theta \leq 180°$) with $\theta = 0°$ being the anterior plane. The positive rotation angle is counterclockwise around the origin. The angle φ represents the polar angle ($90° \leq \varphi \leq 90°$), and $\varphi = 0°$ is defined to be the horizontal plane. The distance from the origin to the tumor surface at (θ, φ) is expressed by the radius $R(\theta, \varphi)$, and radius $R(\theta, \varphi)$ was sampled at 10° intervals in both the polar and the azimuthal directions, giving a total of 684 sampling points. The 3D tumor geometry can be evaluated with the values of $R(\theta, \varphi)$. To enable a visual understanding of the features of the 3D geometry, a 2D surface geometry map like a global map is introduced (Fig. 2). In this map, the values of the tumor radius $R(\theta, \varphi)$ are represented in a color scale and plotted in the θ-φ plane: red indicates the maximum radius and blue the minimum within the tumor. The warm colors (red and yellow) represent convex areas, and cool colors (blue) represent concave areas. If the tumor is a perfect sphere, the map will be uniformly colored (green). This map is termed a surface geometry map. The size of the map was modified to express the tumor volume relative to the pretreatment tumor volume. For example, if the tumor volume decreases to half, the length of each side of the map becomes $(1/2)^{1/3}$.

The patterns of the surface geometry map represent morphologic features of the tumors, and it is possible to know whether the tumor shrinks uniformly by visually comparing maps based on the CT images acquired before and during treatment. Further, to evaluate changes in tumor geometry mathematically, the image correlation between the maps was analyzed. These surface geometry maps were converted into a grayscale with 256 levels; therefore, the intensities of the maps represent the tumor radius and were used in the correlational analysis of the images. The intensities at every position in the map during treatment were compared with those of the corresponding position in the map before treatment, and a correlation coefficient for these two maps was calculated. This image correlation coefficient indicates the similarity of two images, and where the two images are strongly correlated, it suggests that the tumor shrank uniformly.

The changes in tumor location were analyzed as the displacement of the gravitational center of a tumor. To examine the tumor movement during the treatment period, the coordinate systems of the weekly CT scans were translated and rotated so that they corresponded to the pretreatment CT scan using a CT–CT fusion technique. In the 5 patients treated with IMRT, the follow-up and pretreatment CT images were aligned with the reference images by means of the three fiducial markers implanted in the mouthpieces. The accuracy of the patient setup localization using the fiducial markers in the mouthpieces has been reported elsewhere (18). In the patient for whom the mouthpiece was not used, two images were matched based on the bone structure. The displacement of the gravitational center of a tumor was measured in the coordinate system of the pretreatment CT.

RESULTS

Details of changes in tumor volumes during the radiotherapy are shown in Table 2. After irradiation with 66 to 70 Gy, the tumor volumes decreased to 0.31 to 8.4 cm^3 (to 8.7–39 % of the initial volumes). In some cases, the measured tumor

Table 2. Tumor volume changes during treatment. Values in brackets under the sizes of the tumors show the number of days elapsed from start of treatment (negative values are days before start of treatment)

	Absolute (cm^3) and relative (%) tumor volume							
Patient	CT0	CT1	CT2	CT3	CT4	CT5	CT6	CT7
1	3.5 (100%) (Day −20)	2.2 (63%) (Day 12)	1.5 (44%) (Day 19)	1.1 (31%) (Day 26)	0.72 (20%) (Day 33)	0.56 (16%) (Day 40)	0.55 (15%) (Day 48)	0.31 (8.7%) (Day 54)
2	55.1 (100%) (Day –6)	36.5 (66%) (Day 9)	19.1 (35%) (Day 19)	15.9 (29%) (Day 30)	14.3 (26%) (Day 34)	8.4 (15%) (Day 44)		
3	10.4 (100%) (Day –21)	9.5 (91%) (Day 9)	5.3 (51%) (Day 15)	4.1 (39%) (Day 22)	2.8 (27%) (Day 29)	2.5 (24%) (Day 36)	2.2 (21%) (Day 43)	2.4 (23%) (Day 50)
4	7.6 (100%) (Day –19)	7.6 (101%) (Day 7)	4.1 (55%) (Day 14)	3.7 (48%) (Day 21)	3.4 (45%) (Day 28)	3.1 (41%) (Day 35)	2.1 (28%) (Day 42)	1.5 (20%) (Day 49)
5	7.2 (100%) (Day –13)	9.5 (131%) (Day 7)	8.3 (115%) (Day 14)	6.6 (91%) (Day 21)	5.8 (80%) (Day 27)	4.0 (55%) (Day 42)	2.8 (39%) (Day 49)	
6	12.7 (100%) (Day –27)	14.2 (112%) (Day 9)	8.0 (63%) (Day 16)	5.3 (42%) (Day 23)	4.1 (32%) (Day 30)	2.9 (23%) (Day 37)	2.5 (19%) (Day 44)	2.4 (15%) (Day 51)

Abbreviations: CT0 = pretreatment computed tomography images; CT1 = CT images at 1 week; CT2 = CT images at 2 weeks, etc.

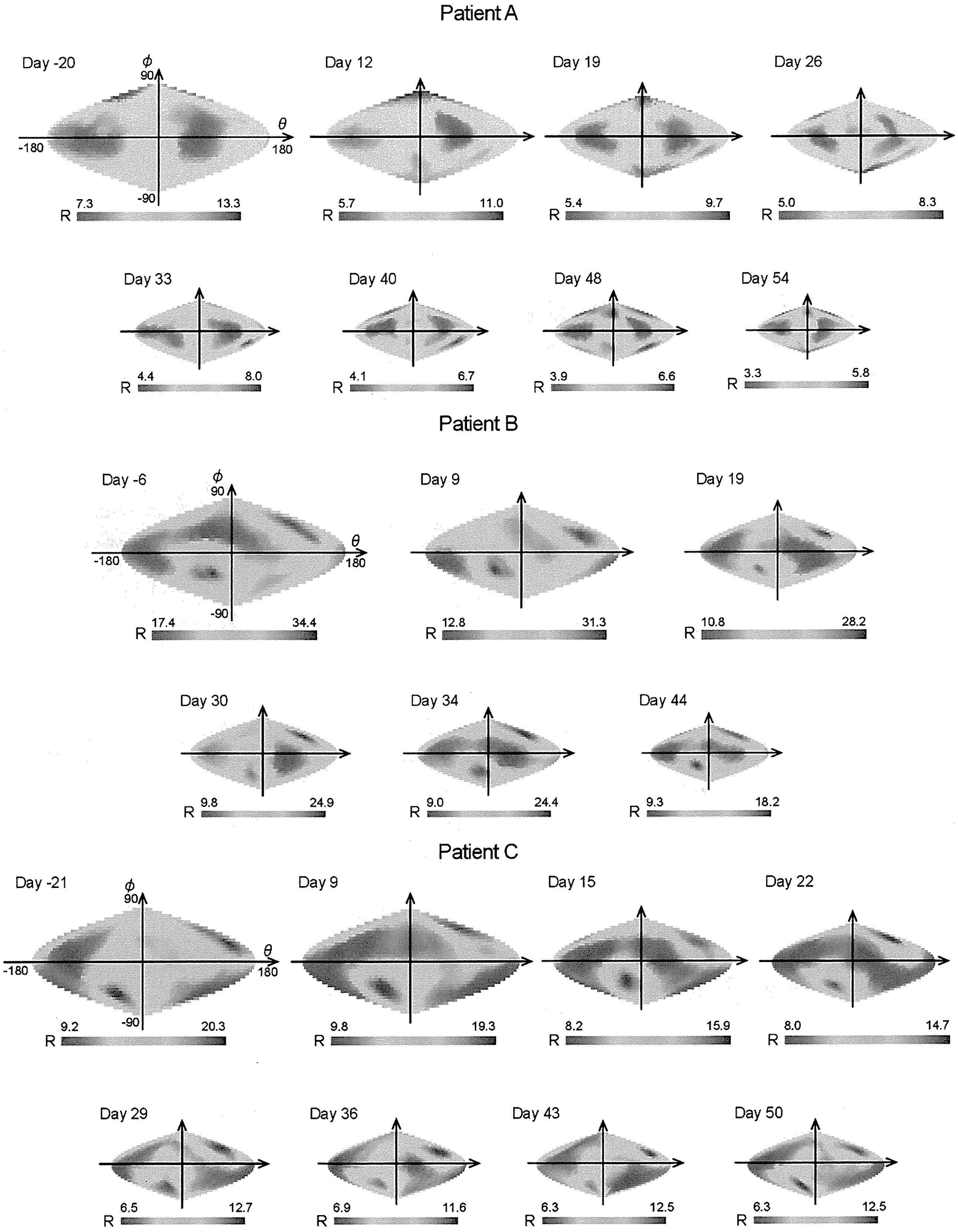

Fig. 3. Changes in three-dimensional tumor geometries during radiotherapy represented using surface geometry maps. Day + number represents the day of the CT examination after the starting date of radiotherapy for patients 1, 2, 3, 4, 5, and 6, respectively. Negative values are days before the start of treatment.

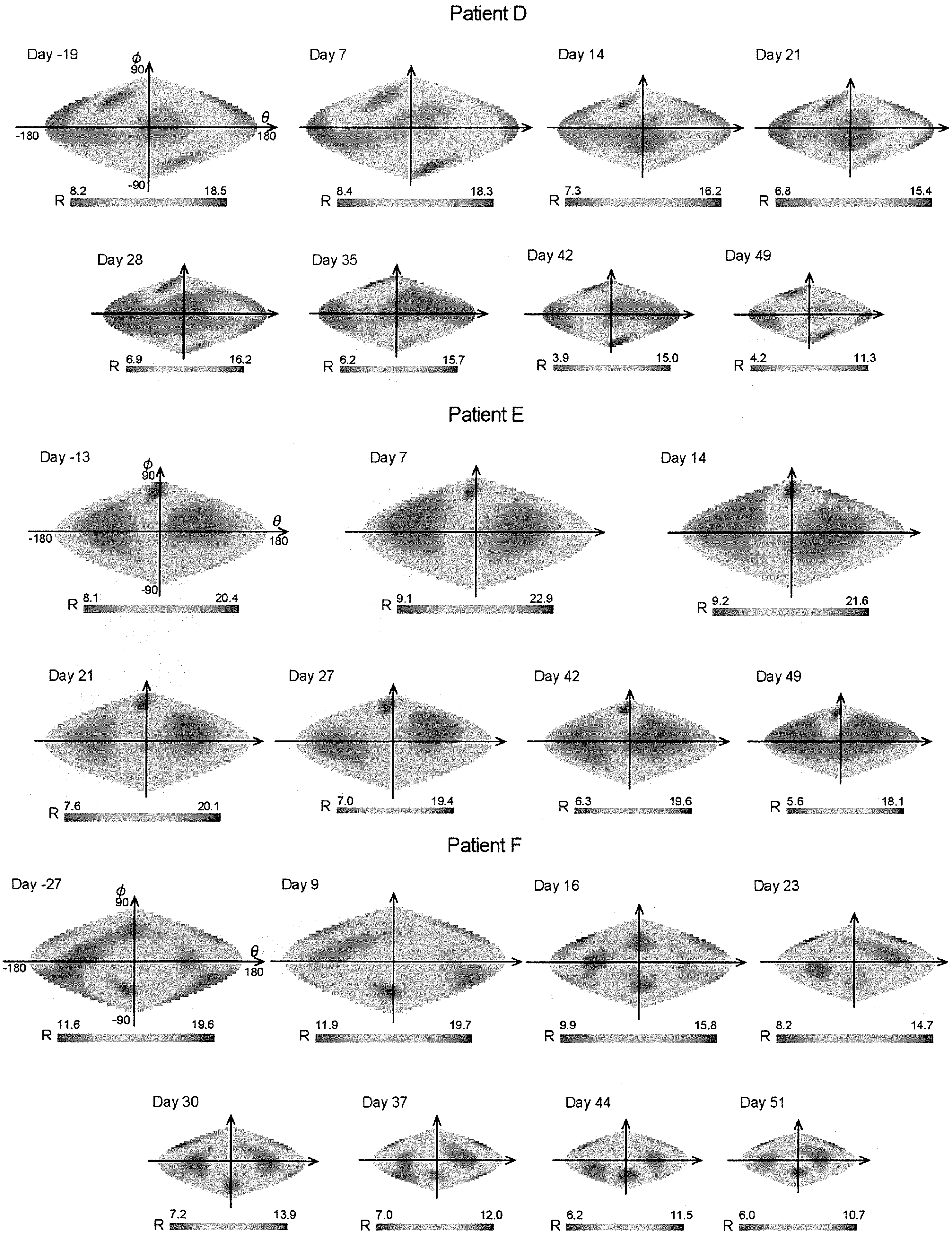

Fig. 3. (*continued*).